

Perpendicular magnetic anisotropy in ultra-thin Cu₂Sb-type (Mn-Cr)AlGe films onto thermally oxidized silicon substrates

Takahide Kubota,^{1, 2, a)} Keita Ito,^{1, 2} Rie Y Umetsu,^{1, 2, 3} and Koki Takanashi^{1, 2, 3}

¹⁾*Institute for Materials Research, Tohoku University, Sendai 980-8577, Japan*

²⁾*Center for Spintronics Research Network, Tohoku University, Sendai 980-8577, Japan*

³⁾*Center for Science and Innovation in Spintronics (Core Research Cluster), Tohoku University, Sendai 980-8577, Japan*

(Dated: 1 March 2025)

Perpendicularly magnetized films showing small saturation magnetization, M_s , are essential for spin-transfer-torque writing type magnetoresistive random access memories, STT-MRAMs. An intermetallic compound, (Mn-Cr)AlGe of the Cu₂Sb-type crystal structure was investigated, in this study, as a material showing the low M_s (~ 300 kA/m) and high-perpendicular magnetic anisotropy, K_u . The layer thickness dependence of K_u and effects of Mg-insertion layers at top and bottom (Mn-Cr)AlGe|MgO interfaces were studied in film samples fabricated onto thermally oxidized silicon substrates to realize high- K_u in the thickness range of a few nanometer. Optimum Mg-insertion thicknesses were 1.4 and 3.0 nm for the bottom and the top interfaces, respectively, which were relatively thick compared to results in similar insertion effect investigations on magnetic tunnel junctions reported in previous studies. The cross-sectional transmission electron microscope images revealed that the Mg-insertion layers acted as barriers to interdiffusion of Al-atoms as well as oxidization from the MgO layers. The values of K_u were about 7×10^5 and 2×10^5 J/m³ at room temperature for 5 and 3 nm-thick (Mn-Cr)AlGe films, respectively, with the optimum Mg-insertion thicknesses. The K_u at a few nanometer thicknesses is comparable or higher than those reported in perpendicularly magnetized CoFeB films which are conventionally used in MRAMs, while the M_s value is one third or less smaller than those of the CoFeB films. The developed (Mn-Cr)AlGe films are promising from the viewpoint of not only the magnetic properties, but also the compatibility to the silicon process in the film fabrication.

^{a)}takahide.kubota@tohoku.ac.jp; author to whom correspondence should be addressed.

Magnetoresistive random access memory, MRAM, is an emerging memory attracting much interest in its non-volatility and fast operation.¹⁻³ For expanding practical application of MRAMs, reduction of the critical current density, J_c , is required for the magnetization switching induced by spin-transfer-torque, STT, in magnetic tunnel junctions, MTJs. The J_c is proportional to saturation magnetization, M_s of the magnetization switching layer⁴, thus magnetic materials showing low M_s are important. For the STT-MRAMs with giga-bit-class memory capacity, in addition, perpendicular magnetization is essential for small J_c ^{5,6} as well as for high-density memory cells, and the high perpendicular magnetic anisotropy, K_u , is also necessary for the data retention.¹⁻³ Various materials have been studied as a class of low M_s and high K_u system, *e.g.* Mn-Ga alloys showing D0₂₂- and L1₀-phases,⁷⁻⁹ D0₂₂-Mn₃Ge alloys,¹⁰⁻¹² and a body-centered-tetragonal Mn ultra-thin film.¹³ Although attractive properties were reported for all those materials showing $M_s \sim 100 - 300$ kA/m and $K_u \sim 10^6$ J/m³ or greater at room temperature, a drawback is that most studies were done using single crystalline MgO substrates which are unsuitable for practical devices. A few studies also reported film samples onto thermally oxidized silicon substrates, *e.g.* using Mn-Ga alloys,^{14,15} however, another intrinsic drawback is all those Mn-alloys in previous studies were ferrimagnets¹⁶ which caused reduction of spin polarization at the interface.¹⁷

As an alternative material with the Mn-alloys in previous studies, here, an intermetallic compound (Mn-Cr)AlGe¹⁸ is focused on. The (Mn-Cr)AlGe compound is a ferromagnet which belongs to a family of Mn-based intermetallic compounds showing the Cu₂Sb-type crystal structure, such as MnAlGe¹⁸⁻²² and MnGaGe.^{20,23,24} The M_s values of the Mn-compounds range 200 – 300 kA/m which are relatively small because of the small magnetic moment of the ferromagnetically coupled Mn-moments showing itinerant electronic structure.²⁵ The values of K_u are 7.3×10^5 and 8.1×10^5 J/m³ for (Mn_{0.76}Cr_{0.28})Al_{0.94}Ge_{1.02}¹⁸ and for Mn_{1.0}Ga_{1.1}Ge_{0.9}²⁴, respectively, at room temperature, which are much higher than those reported for conventionally used CoFeB films showing perpendicular magnetization.²⁶ These physical properties of low M_s and high K_u are promising for the MRAM application, in addition, there is another merit of the silicon process compatibility for those compounds, *i.e.* the films with (001)-texture exhibiting perpendicular magnetization are available on the SiO₂ surfaces as well as other amorphous substrates.^{18,22,27-30} The (001)-orientation is also an essential requirement for MTJs using (001)-textured MgO|CoFe(B) structure that exhibits large tunnel magnetoresistance.³¹ In addition, a recent study simulated reduction of J_c in antiferromagnetically coupled layered structure consisting of high- and low- M_s ma-

terials,³² for which the Cu₂Sb-type (Mn-Cr)AlGe can be a low- M_s material layered with, *e.g.*, CoFe(B) showing relatively high- M_s . In our previous study, the template effect was demonstrated for the (001)-textured growth of the Cu₂Sb-MnAlGe films using (001)-textured MgO seed/capping layers, in which the MgO(001) template promotes the (001)-texture in the MnAlGe films, however, relatively thick dead layer around the MnAlGe|MgO interfaces degraded K_u for the thickness less than 10 nm.³³ The sputtered MgO layer may cause oxidation at the interface with a metallic magnetic material, which can be eliminated by inserting an ultra-thin metallic layer, *e.g.* a Mg-layer in between.^{34–36} Such an interface layer possibly improves the dead layer problem of the interface between the Mn-compounds and MgO, thus in this study, the effect of the Mg-interface layer was investigated for (Mn-Cr)AlGe|MgO interfaces to realize high- K_u at the layer thickness of a few nanometer.

The layered film samples were fabricated using a magnetron sputtering system with a base vacuum pressure bellow 1×10^{-7} Pa for the deposition chamber. All samples were fabricated onto single crystalline silicon (100) substrates with a 650 nm-thick thermally oxidized amorphous layer on the surface. The stacking structure of samples is as follows: Sub.|buffer layers|MgO 1.5 nm|Mg $t_{\text{Mg}}^{\text{btm}}$ |(Mn-Cr)AlGe t | Mg $t_{\text{Mg}}^{\text{top}}$ |MgO 1.5 nm|cap, where $t_{\text{Mg}}^{\text{btm}(\text{top})}$ and t are the thicknesses of the Mg-insertion for the bottom (top) interface and that of the (Mn-Cr)AlGe layer, respectively. The buffer layers consist of Ta 3 nm|W 0.3 nm|CoFeBTa 1 nm, from bottom to top, which promotes (001)-texture of the bottom MgO layer.³⁷ Note that the CoFeBTa layer is nonmagnetic in this study. The film composition of the (Mn-Cr)AlGe layer was (Mn_{0.8}Cr_{0.2})Al_{1.1}Ge_{0.9} in the atomic ratio. All layers were deposited at room temperature inside the ultra-high vacuum chamber, and a 3 nm-thick Ta was deposited on the top as a cap layer. After the capping, all samples were annealed using a vacuum furnace. The annealing temperatures were 300, 400, and 500 °C. Magnetization curves were measured at room temperature using vibration sample magnetometers and a superconducting quantum interference device magnetometer. The interface properties as well as the crystal structures were characterized using high-angle annular dark field-, HAADF-, scanning transmission electron microscope, STEM, images. The thicknesses of the Mg-insertion were optimized via two steps: First, the top interface was optimized by changing $t_{\text{Mg}}^{\text{top}}$ from 0 to 7 nm, for which $t_{\text{Mg}}^{\text{btm}}$ was fixed to 0. Then, for the second step, the bottom interface was optimized with the $t_{\text{Mg}}^{\text{btm}}$ in the range of 0 to 1.4 nm, for which $t_{\text{Mg}}^{\text{top}}$ was fixed to 3.0 nm. For both steps, t was fixed to 10 nm. After the two steps, three sample series were selected as shown in Table I to study the t dependence of K_u for the (Mn-Cr)AlGe layer, for which t was changed from

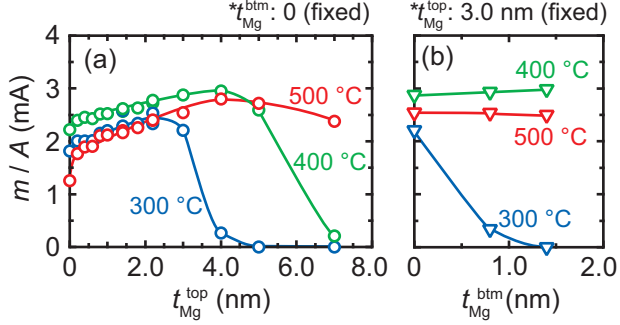


FIG. 1. Mg-insertion thickness, $t_{\text{Mg}}^{\text{top}}$ or $t_{\text{Mg}}^{\text{btm}}$, dependence of magnetization values, m , per the sample area, A . The $t = 10$ nm for all samples. (a) In the $t_{\text{Mg}}^{\text{top}}$ dependence, $t_{\text{Mg}}^{\text{btm}}$ was fixed to 0, and (b) in the bottom $t_{\text{Mg}}^{\text{btm}}$ dependence, $t_{\text{Mg}}^{\text{top}}$ was fixed to 3.0 nm. The temperatures shown in the panels are the annealing temperatures of the samples.

TABLE I. Definition of the sample series.

| Series | Mg layer thickness (nm) | |
|--------|-------------------------|-----|
| | bottom | top |
| A | 0 | 0 |
| B | 0 | 3.0 |
| C | 1.4 | 3.0 |

3 to 30 nm. The Mg-insertion dependence of magnetization, m , per the sample area, A , is shown in figure 1.³⁸ For the top interface, shown in fig. 1(a), the magnetization increases with $t_{\text{Mg}}^{\text{top}}$ of up to the certain thickness values depending on the annealing temperature, *i.e.*, the values of $t_{\text{Mg}}^{\text{top}}$ for the maximum m/A shift towards larger values for the higher annealing temperature, the reason for which will be discussed in the latter part of this article. The maximum m/A was about 2.9 mA for $t_{\text{Mg}}^{\text{top}} = 3 - 4$ nm and the annealing temperature of 400 °C, thus $t_{\text{Mg}}^{\text{top}}$ of 3.0 nm is selected as an optimum value for the first step. The Mg-insertion for the bottom interface, shown in fig. 1(b), exhibits moderate dependence except for the annealing temperature of 300 °C in which m/A monotonically decreases with $t_{\text{Mg}}^{\text{btm}}$. For other annealing temperatures, with increasing $t_{\text{Mg}}^{\text{btm}}$, m/A gradually increases for 400 °C, while that exhibits gradual decrease for 500 °C. As a conclusion from the second step, the $t_{\text{Mg}}^{\text{btm}}$ of 1.4 nm is selected.

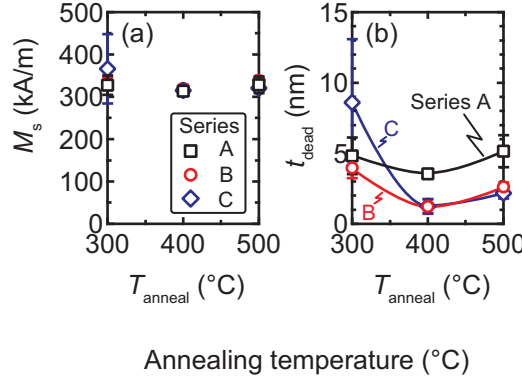


FIG. 2. Annealing temperature dependence of (a) saturation magnetization, M_s and the thicknesses of dead layer, t_{dead} evaluated using the t dependence of m/A plots.

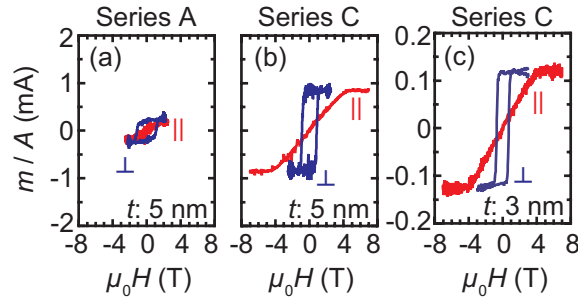


FIG. 3. Magnetization curves of 5 nm-thick samples for (a) series A and (b) C. (c) a 3 nm-thick sample for series C. The annealing temperature is 400 °C for all samples. The marks of \perp and \parallel represent applied magnetic fields of perpendicular-to-plane and in-plane directions, respectively.

Three sample series listed in table I are selected for the investigation on the t dependence of K_u . The M_s and the dead layer thickness, t_{dead} were evaluated by the slope and the intercept to the horizontal axis, respectively, in plots of m/A as a function of t .³⁹ The values are summarized in figure 2. The M_s shows no dependence on the sample series or annealing temperature within the range of error bars, and the values are about 330 kA/m which is close to a theoretical value of 352 kA/m for $(\text{Mn}_{0.8}\text{Cr}_{0.2})\text{AlGe}$.¹⁸ On the other hand, t_{dead} shows clear dependence on the sample series as well as the annealing temperature: On the annealing temperature dependence, t_{dead} exhibit minima at 400 °C for all sample series, and among the sample series, series B and C exhibit the minima; t_{dead} of about 1.2 ± 0.5 nm which is smaller than that of 3.5 ± 0.2 nm for the series A. The difference among the sample series is clearly seen in magnetic properties especially at t below 10 nm. Figure 3 shows magnetization curves of 5 nm-thick samples for series A and C, and a 3 nm-thick samples

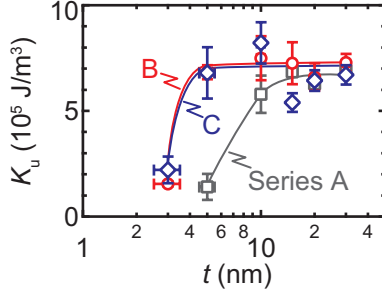


FIG. 4. The t dependence of perpendicular magnetic anisotropy energy, K_u .

for series C. The squareness of hysteresis curves for the perpendicular-to-plane magnetic field direction is close to one for both 5 nm-thick samples of series A and C; however, the magnitude of magnetization is smaller for the sample in series A (fig. 3(a)) than that in series C (fig. 3(b)). In the series C, the perpendicular magnetization showing a high squareness ratio is maintained down to the t of 3 nm as shown in fig. 3(c). Note that similar results were obtained in series B for $t = 5$ and 3 nm which are shown in Supplementary Material. The t dependence of K_u was evaluated to characterize the difference among the sample series quantitatively. The K_u is defined using the actual layer thickness, $t - t_{\text{dead}}$, with the following equation, $K_u = K_u^{\text{eff}}/(t - t_{\text{dead}}) + (\mu_0/2)M_s^2$, where K_u^{eff} is the effective perpendicular magnetic anisotropy energy per unit area which was calculated from the area enclosed by the perpendicular-to-plane and in-plane magnetization curves, e.g. shown in fig. 3. The K_u are summarized in figure 4 as a function of t for all the sample series. For series A, K_u of about 7×10^5 J/m³ was achieved in samples down to the t of 15 nm, and at the t of 10 nm or thinner, K_u decreases with decreasing t , which is about 1×10^5 J/m³ at 5 nm. On the other hand for series B and C, K_u of about 7×10^5 J/m³ was maintained down to the t of 5 nm; in addition, 3 nm-thick samples show K_u of about 2×10^5 J/m³. These results clearly confirm that the reduction of t_{dead} efficiently improved the K_u in a few nanometer thickness region. Although the Mg-insertion is found to be useful for suppressing the t_{dead} , a question is the relatively thick $t_{\text{Mg}}^{\text{top(btm)}}$, *i.e.*, in previous studies using MgO-MTJs, the optimum thicknesses of Mg-insertion range 0.4 – 1 nm.^{34–36} In the present study, the optimum thicknesses are 1.4 and 3 nm for the bottom and top (Mn-Cr)AlGe|MgO interfaces, respectively, which are thicker than those in the previous studies. The cross sectional HAADF-STEM observations were carried out to characterize the dead layer and the crystal structures more clearly, and the images are shown in figure 5 for $t = 10$ nm in series A and B. First, concerning crystal structure of the middle region, both samples exhibit high-(001) orientation which can be seen

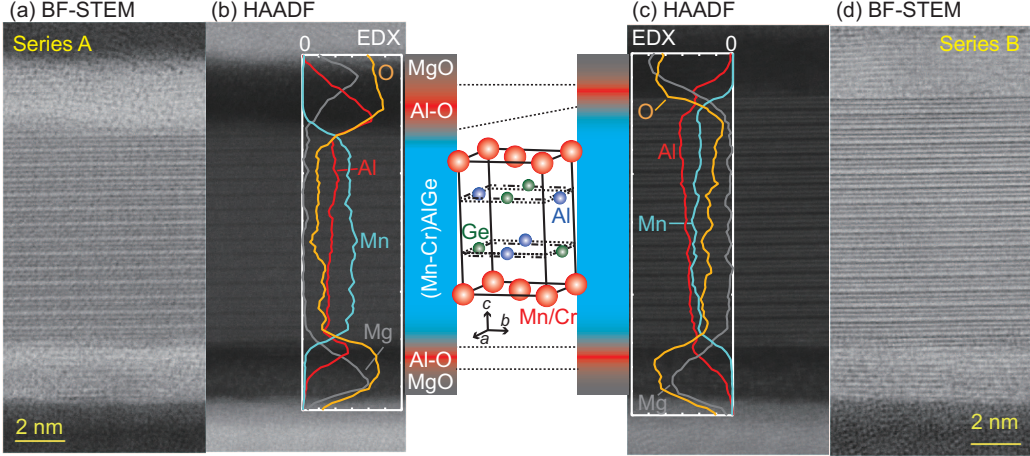


FIG. 5. The cross-sectional scanning transmission electron microscope, STEM, images of samples for (a, b) series A and (c, d) B. The annealing temperature was 400 °C and $t = 10$ nm for both samples. (a, d) The bright field, BF, images. (b, c) high-angle annular dark field, HAADF, images. The lines drawn inside the HAADF images are line profiles of energy dispersive x-ray mapping for the samples. The color bars drawn on the middle describe the possible layer components. Crystal structure of the Cu₂Sb-type (Mn-Cr)AlGe is schematically depicted in the center.

in the lattice images of the bright field-, BF-, STEM images shown in figs. 5(a) and 5(d) for series A and B, respectively. The high-orientation can be also confirmed in HAADF images shown in figs. 5(b) and 5(c) in which periodical contrast changes are clearly observed. The HAADF contrasts also implies the layered atomic components with the chemical order as shown in the center of fig. 5. Second, a difference is found for the actual layer thickness of the (Mn-Cr)AlGe layer: From the BF-STEM images, the layer thicknesses are 8.5 ± 0.2 and 9.7 ± 0.2 nm for series A and B, respectively. Line profiles of energy dispersive x-ray, EDX, spectroscopy represent the difference in the upper interfaces more clearly, which causes the difference in the layer thicknesses: For the series A sample, Al-rich oxidized region is found between the (Mn-Cr)AlGe and the top-MgO layer, for which the thickness is approximately 2 nm and is marked as "Al-O" in the color scale beside the HAADF image of fig. 5(b). On the other hand for series B, similar Al-rich region is observed at the top interface, however, the thickness of less than 1 nm is much smaller than that in series A. Concerning the interface to the bottom MgO layer, the Al-O layer is also observed in each sample series, for which the thickness of approximately 1 nm is similar to each other. Such formation of the Al-O layer caused by interdiffusion of Al-atoms from a metallic layer to an oxide layer has been reported in layered samples consisting of an ultra-thin Co₂FeAl film capped by a sputtered

MgO layer, in which the diffusion of Al-atoms might occur during the deposition of the MgO upper layer onto the metallic layer containing Al. In the present study, the formation of the Al-O layer can be qualitatively understood with the following scenario: The (Mn-Cr)AlGe layer is amorphous in the as-deposited state, for which the constituent elements are randomly distributed at the surface before the deposition of the MgO layer. During the deposition of the MgO layer, the surface of (Mn-Cr)AlGe could be exposed to small amount of oxygen plasma which causes oxygen rich interface between the (Mn-Cr)AlGe and the top MgO layers. Here, the formation free energy of Al-oxide is the smallest among the constituent elements of (Mn-Cr)AlGe⁴⁰, thus Al diffusion may occur with assistant of plasma energy during the deposition of MgO as well as the post-annealing procedure resulting in the formation of the Al-rich oxide region for the upper interface. For the bottom interface, Al diffusion may also occur during the annealing process, however, the amount of Al-diffusion is less than the top interface because the oxygen rich interface was never formed for the bottom interface. Thus, the Mg-insertion is considered to suppress such Al-diffusion as well as the formation of Al-O resulting in the suppression of t_{dead} and the enhancement of K_u at t in a few nanometer thickness region. Based on the discussion above, an answer can be given to the question for the different optimum $t_{\text{Mg}}^{\text{top(btm)}}$ values depending on the annealing temperatures shown in fig. 1: By considering that the diffusion process of Al is a factor which promotes the crystallization of (Mn-Cr)AlGe, for no Mg-insertion sample, Al atoms move inside the layer by relatively low energy-assist, *i.e.* the low annealing temperature of 300 °C which is sufficient for crystallization. However, with increasing the Mg-insertion, the Al-diffusion was suppressed, which requires the annealing temperature of 400 °C or higher for crystallization showing large magnetization.

To conclude, the perpendicular magnetic anisotropy of the Cu₂Sb-type (Mn-Cr)AlGe films was investigated, especially focusing on a-few-nanometer-thickness region of the (Mn-Cr)AlGe layer. The Mg-insertion layer was employed at the (Mn-Cr)AlGe|MgO interfaces, for which effects on magnetic properties and the t_{dead} were systematically examined. The M_s exhibited almost no dependence on the Mg-insertion thickness, while t_{dead} reduced with the Mg-insertion. The cross-sectional HAADF-STEM images presented clear contrast change for the (Mn-Cr)AlGe layer, which represented highly oriented (001)-crystal planes as well as chemical order of (Mn-Cr)AlGe. The STEM images also revealed role of the Mg-insertion as a diffusion barrier to Al atoms. The K_u of about 7×10^5 J/m³ at t of 5 nm is comparable with those for thick, *e.g.* t of 30 nm samples, and much higher than those reported in perpendicu-

larly magnetized CoFeB films which are conventionally used in STT-MRAMs. Although K_u of about 2×10^5 J/m³ at t of 3 nm is comparable with those for the CoFeB films, the small M_s of (Mn-Cr)AlGe can be a merit for reducing the J_c . Among various materials showing small- M_s and high- K_u , another merit of (Mn-Cr)AlGe is the silicon process compatibility: All the samples in this study were fabricated using thermally oxidized silicon substrates with relatively thin underlayers including the (001)-oriented MgO template.³³ The solid-phase-epitaxy based method for crystallization is compatible with device fabrication process for complementary metal oxide semiconductor devices as well as for MTJs.³¹ The (Mn-Cr)AlGe film showing perpendicular magnetization is also interesting from the application point of view.

ACKNOWLEDGMENTS

TK would like to thank Dr. Yoshiaki Sonobe for fruitful discussion, Mr. Issei Narita for technical support of film composition analysis, and the Foundation for Promotion of Material Science and Technology of Japan for HAADF-STEM observation and analysis. This work was partially supported by KAKENHI (20K05296) from JSPS, and a cooperative research program (No.20G0414) of the CRDAM-IMR, Tohoku Univ.

DATA AVAILABILITY STATEMENTS

The data that support the findings of this study are available within its supplementary material.

REFERENCES

¹S. Bhatti, R. Sbiaa, A. Hirohata, H. Ohno, S. Fukami, and S. Piramanayagam, Mater Today **20**, 530 (2017).

²S. Ikegawa, F. B. Mancoff, J. Janesky, and S. Aggarwal, IEEE Transactions on Electron Devices **67**, 1407 (2020).

³T. Na, S. H. Kang, and S.-O. Jung, IEEE Transactions on Circuits and Systems II: Express Briefs **68**, 12

⁴J. Slonczewski, J. Magn. Magn. Mater. **159**, L1 (1996).

⁵T. Kishi, H. Yoda, T. Kai, T. Nagase, E. Kitagawa, M. Yoshikawa, K. Nishiyama, T. Daimon, M. Nagamine, M. Amano, S. Takahashi, M. Nakayama, N. Shimomura, H. Aikawa,

S. Ikegawa, S. Yuasa, K. Yakushiji, H. Kubota, A. Fukushima, M. Oogane, T. Miyazaki, and K. Ando, in *2008 IEEE International Electron Devices Meeting* (IEEE, 2008).

⁶H. Yoda, T. Kishi, T. Nagase, M. Yoshikawa, K. Nishiyama, E. Kitagawa, T. Daibou, M. Amano, N. Shimomura, S. Takahashi, T. Kai, M. Nakayama, H. Aikawa, S. Ikegawa, M. Nagamine, J. Ozeki, S. Mizukami, M. Oogane, Y. Ando, S. Yuasa, K. Yakushiji, H. Kubota, Y. Suzuki, Y. Nakatani, T. Miyazaki, and K. Ando, *Curr. Appl Phys.* **10**, e87 (2010).

⁷F. Wu, S. Mizukami, D. Watanabe, H. Naganuma, M. Oogane, Y. Ando, and T. Miyazaki, *Appl. Phys. Lett.* **94**, 122503 (2009).

⁸S. Mizukami, F. Wu, A. Sakuma, J. Walowski, D. Watanabe, T. Kubota, X. Zhang, H. Naganuma, M. Oogane, Y. Ando, and T. Miyazaki, *Phys. Rev. Lett.* **106**, 117201 (2011).

⁹S. Mizukami, T. Kubota, F. Wu, X. Zhang, T. Miyazaki, H. Naganuma, M. Oogane, A. Sakuma, and Y. Ando, *Phys. Rev. B* **85**, 014416 (2012).

¹⁰H. Kurt, N. Baadji, K. Rode, M. Venkatesan, P. Stamenov, S. Sanvito, and J. M. D. Coey, *Appl. Phys. Lett.* **101**, 132410 (2012).

¹¹S. Mizukami, A. Sakuma, A. Sugihara, T. Kubota, Y. Kondo, H. Tsuchiura, and T. Miyazaki, *Appl. Phys Express* **6**, 123002 (2013).

¹²A. Sugihara, S. Mizukami, Y. Yamada, K. Koike, and T. Miyazaki, *Appl. Phys. Lett.* **104**, 132404 (2014).

¹³K. Z. Suzuki, S. Kimura, H. Kubota, and S. Mizukami, *ACS Appl. Mater. & Interfaces* **10**, 43305 (2018).

¹⁴A. Ono, K. Z. Suzuki, R. Ranjbar, A. Sugihara, and S. Mizukami, *Appl. Phys. Express* **10**, 023005 (2017).

¹⁵K. Z. Suzuki, A. Ono, R. Ranjbar, A. Sugihara, and S. Mizukami, *IEEE Trans. Magn.* **53**, 2101004 (2017).

¹⁶Theoretically, $Mn_{50}Ga_{50}$ with the $L1_0$ phase is a ferromagnet. However, in experiments, the film samples were off-stoichiometric with Mn-rich composition which are ferrimagnetic. The stoichiometric $L1_0$ - $Mn_{50}Ga_{50}$ is unstable, thus there were few experimental reports.

¹⁷J. Jeong, Y. Ferrante, S. V. Faleev, M. G. Samant, C. Felser, and S. S. P. Parkin, *Nat. Commun.* **7**, 10276 (2016).

¹⁸T. Kubota, Y. Kota, K. Ito, R. Y. Umetsu, M. Sun, M. Mizuguchi, and K. Takanashi, *Appl. Phys. Express* **12**, 103002 (2019).

¹⁹K. Shibata, H. Watanabe, H. Yamauchi, and T. Shinohara, *J. Phys. Soc. Jpn.* **35**, 448 (1973).

²⁰R. Y. Umetsu, Y. Mitsui, I. Yuito, T. Takeuchi, and H. Kawarada, IEEE Trans. Magn. **50**, 1001904 (2014).

²¹S. Mizukami, A. Sakuma, T. Kubota, Y. Kondo, A. Sugihara, and T. Miyazaki, Appl. Phys. Lett. **103**, 142405 (2013).

²²T. Kubota, Y. Kota, K. Ito, R. Y. Umetsu, M. Sun, M. Mizuguchi, and K. Takanashi, AIP Adv. **10**, 015122 (2020).

²³J. Goodenough, G. Street, K. Lee, and J. Suits, J. Phys. Chem. Solids **36**, 451 (1975).

²⁴M. Sun, T. Kubota, K. Ito, S. Takahashi, Y. Hirayama, Y. Sonobe, and K. Takanashi, Appl. Phys. Lett. **116**, 062402 (2020).

²⁵K. Motizuki, H. Ido, T. Itoh, and M. Morifuji, *Electronic Structure and Magnetism of 3d-Transition Metal Pnictides* (Springer Berlin Heidelberg, 2010).

²⁶S. Ikeda, K. Miura, H. Yamamoto, K. Mizunuma, H. D. Gan, M. Endo, S. Kanai, J. Hayakawa, F. Matsukura, and H. Ohno, Nat. Mater. **9**, 721 (2010).

²⁷E. Sawatzky and G. B. Street, J. Appl. Phys. **44**, 1789 (1973).

²⁸R. C. Sherwood, E. A. Nesbitt, J. H. Wernick, D. D. Bacon, A. J. Kurtzig, and R. Wolfe, J. Appl. Phys. **42**, 1704 (1971).

²⁹K. Lee and J. C. Suits, *AIP Conference Proceedings*, AIP Conf. Proc. **10**, 1429 (1973).

³⁰M. Sun, *Magnetic properties of C38-type Mn-based intermetallic compound films for spintronic applications*, PhD thesis, Tohoku University (2020).

³¹S. Yuasa and D. D. Djayaprawira, J. Phys. D: Appl. Phys. **40**, R337 (2007).

³²K. Yamada, K. Kubota, and Y. Nakatani, J. Appl. Phys. **127**, 133906 (2020).

³³T. Kubota, K. Ito, R. Y. Umetsu, M. Mizuguchi, and K. Takanashi, AIP Adv. **11**, 015124 (2021).

³⁴K. Tsunekawa, D. D. Djayaprawira, M. Nagai, H. Maehara, S. Yamagata, N. Watanabe, S. Yuasa, Y. Suzuki, and K. Ando, Appl. Phys. Lett. **87**, 072503 (2005).

³⁵Y. Sakuraba, M. Hattori, M. Oogane, H. Kubota, Y. Ando, A. Sakuma, N. D. Telling, P. Keatley, G. van der Laan, E. Arenholz, R. J. Hicken, and T. Miyazaki, J. Magn. Soc. Jpn. **31**, 338 (2007).

³⁶T. Kubota, S. Mizukami, D. Watanabe, F. Wu, X. Zhang, H. Naganuma, M. Oogane, Y. Ando, and T. Miyazaki, J. Appl. Phys. **110**, 013915 (2011).

³⁷The 0.3 nm-thick W layer was not used in the series A samples, however, no difference in magnetic properties was confirmed by comparing the samples with- and without- the W

layer, which are shown in Supplementary Material.

³⁸Magnetization curves for fig. 1 appear in Supplementary Material.

³⁹Magnetization curves and the plots of m/A vs t used for fig. 2 are shown in Supplementary Material.

⁴⁰H. J. T. Ellingham, J. Soc. Chem. Ind. **63**, 125 (1944).